The Astrophysical Journal, 748:26 (12pp), 2012 March 20 doi:10.1088/0004-637X/748/1/26

X-RAY OBSERVATIONS OF THE NEW UNUSUAL MAGNETAR SWIFT J1834.9−0846

Oleg Kargaltsev[1], Chryssa Kouveliotou[2], George G. Pavlov[3,4], Ersin Göğüş[5], Lin Lin[5], Stefanie Wachter[6], Roger L. Griffith[6], Yuki Kaneko[5], and George Younes[2,7]
[1] Department of Astronomy, Bryant Space Science Center, University of Florida, Gainesville, FL 32611, USA; oyk100@astro.ufl.edu
[2] Science & Technology Office, ZP12, NASA/Marshall Space Flight Center, Huntsville, AL 35812, USA
[3] Department of Astronomy and Astrophysics, Pennsylvania State University, 525 Davey Lab, University Park, PA 16802, USA
[4] St.-Petersburg State Polytechnical University, Polytekhnicheskaya ul. 29, 195251, St.-Petersburg, Russia
[5] Faculty of Engineering and Natural Sciences, Sabancı University, Orhanlı-Tuzla, İstanbul 34956, Turkey
[6] Infrared Processing and Analysis Center, California Institute of Technology, Pasadena, CA 91125, USA
[7] Universities Space Research Association, 6767 Old Madison Pike, Suite 450, Huntsville, AL 35806, USA
Received 2011 November 1; accepted 2012 January 9; published 2012 March 1

ABSTRACT

We present X-ray observations of the new transient magnetar Swift J1834.9−0846, discovered with the *Swift* Burst Alert Telescope on 2011 August 7. The data were obtained with *Swift*, *Rossi X-ray Timing Explorer* (*RXTE*), *CXO*, and *XMM-Newton* both before and after the outburst. Timing analysis reveals single peak pulsations with a period of 2.4823 s and an unusually high pulsed fraction, 85% ± 10%. Using the *RXTE* and *CXO* data, we estimated the period derivative, $\dot{P} = 8 \times 10^{-12}$ s s^{-1}, and confirmed the high magnetic field of the source, $B = 1.4 \times 10^{14}$ G. The decay of the persistent X-ray flux, spanning 48 days, is consistent with a power law, $F \propto t^{-0.5}$. In the *CXO*/Advanced CCD Imaging Spectrometer image, we find that the highly absorbed point source is surrounded by extended emission, which most likely is a dust scattering halo. Swift J1834.9−0846 is located near the center of the radio supernova remnant W41 and TeV source HESS J1834−087. An association with W41 would imply a source distance of about 4 kpc; however, any relation to the HESS source remains unclear, given the presence of several other candidate counterparts for the latter source in the field. Our search for an IR counterpart of Swift J1834.9−0846 revealed no source down to $K_s \sim 19.5$ within the 0.″6 *CXO* error circle.

Key words: gamma-ray burst: individual (HESS J1834−087) – ISM: individual objects (W41) – stars: neutron – X-rays: individuals (Swift J1834.9−0846) – X-rays: ISM

Online-only material: color figures

1. INTRODUCTION

The population of magnetars has been growing rapidly in the last five years, reaching 24 objects as of 2011 August. Originally comprised of soft gamma repeaters (SGRs) and anomalous X-ray pulsars (AXPs; Woods & Thompson 2006), the magnetar population now includes a few more neutron star (NS) groups that have been acknowledged as magnetar candidates. Most of these NSs are slow rotators emitting multiple, very short (a few times 100 ms) hard X-ray/soft γ-ray bursts. Their X-ray luminosities are likely powered by the decay of their high magnetic fields (up to $B \sim 10^{15}$ G), rather than rotational energy losses due to their gradual spin-down (Paczyński 1992; Duncan & Thompson 1992; Thompson & Duncan 1995, 1996). The current synergy between NASA's three observatories (*RXTE*, *Swift*, and *Fermi*) has enabled a much higher rate of discovery of these objects in the last three years. During 2011 July–August alone, two new candidate magnetars were discovered in X-rays, Swift J1822.3−1606 and Swift J1834.9−0846, when they triggered the *Swift*/Burst Alert Telescope (BAT) and the *Fermi*/Gamma-ray Burst Monitor (GBM). Their timing properties were subsequently established with *Rossi X-ray Timing Explorer* (*RXTE*) observations, clinching their magnetar nature. We report here on the X-ray spectral and temporal properties of the latter source.

Swift J1834.9−0846 was discovered on 2011 August 7, when a soft, short burst from the source triggered the BAT at 19:57:46 UT (D'Elia et al. 2011; Halpern 2011); approximately 3.3 hr later, at 23:16:24.91 UT, another SGR-like burst triggered GBM from the general direction of the earlier BAT location (Guiriec et al. 2011). Although the GBM location included a large area with several magnetar sources, the near time coincidence and the X-ray properties of these events pointed to a common origin of a new source (Barthelmy et al. 2011). The source triggered the BAT again on 2011 August 30 at 23:41:12 UT (Hoversten et al. 2011).

Optical observations of the field ∼16 minutes after the BAT trigger with the Special Astrophysical Observatory/Big Telescope Alt-azimuth 6 m telescope detected an object at magnitude $R_c = 23.44 \pm 0.34$ (Moskvitin et al. 2011). Simultaneous observations with the 1.5 m Observatorio de Sierra Nevada telescope in the *I* band did not detect that object to a limit of $I = 21.6$ (Tello et al. 2011). Archival IR images of the region as part of the UKIDSS Galactic Plane Survey (Lucas et al. 2008) in the *J*, *H*, and *K* bands on 2007 May 10 revealed two sources close to the *Swift*/X-ray Telescope (XRT) location of Swift J1834.9−0846 (Levan & Tanvir 2011). None of these objects coincided with the very precise X-ray position subsequently derived from our *Chandra* Target of Opportunity (ToO) observation (Göğüş et al. 2011b).

RXTE/Proportional Counter Array (PCA) observations of the source on 2011 August 9–10 detected a coherent pulsation at $\nu = 0.402853(2)$ Hz, which corresponded to a spin period $P = 2.482295$ s (Göğüş & Kouveliotou 2011a); this result was later confirmed with our *Chandra* ToO observation on 2011 August 22 (Göğüş et al. 2011b). Continuous *RXTE* monitoring of the source over a time span of two weeks revealed a spin-down rate $\dot{\nu} = -1.3(2) \times 10^{-12}$ Hz s^{-1} (Kuiper & Hermsen 2011). The corresponding estimate of the surface magnetic

Table 1
X-ray Observations of Swift J1834.9−0846

Date	ObsID	Observatory/Detector (Mode)	Exposure (ks)	Time Resolution (s)
2005 Sep 18	0302560301	*XMM-Newton* EPIC	18.6	0.072
2009 Jun 7	10126	*CXO* ACIS-S	46.5	3.2
2011 Aug 7	00458907000	*Swift*/XRT (PC)	1.54	2.5
2011 Aug 7[a]	00458907001	*Swift*/XRT (WT)	0.096	1.8×10^{-3}
2011 Aug 8[a]	00458907002	*Swift*/XRT (WT)	0.129	1.8×10^{-3}
2011 Aug 8	00458907003	*Swift*/XRT (WT)	1.65	1.8×10^{-3}
2011 Aug 8	00458907004	*Swift*/XRT (WT)	0.958	1.8×10^{-3}
2011 Aug 9	00458907006	*Swift*/XRT (WT)	2.67	1.8×10^{-3}
2011 Aug 9	96434-01-01-00	*RXTE* PCA	3.40	9×10^{-7}
2011 Aug 9	96434-01-02-00	*RXTE* PCA	9.66	9×10^{-7}
2011 Aug 12	00458907007	*Swift*/XRT (WT)	5.67	1.8×10^{-3}
2011 Aug 14	00458907008	*Swift*/XRT (WT)	5.39	1.8×10^{-3}
2011 Aug 14	96434-01-03-00	*RXTE* PCA	6.78	9×10^{-7}
2011 Aug 18	96434-01-03-01	*RXTE* PCA	6.75	9×10^{-7}
2011 Aug 18	00458907009	*Swift*/XRT (WT)	5.73	1.8×10^{-3}
2011 Aug 21	00458907010	*Swift*/XRT (WT)	2.49	1.8×10^{-3}
2011 Aug 22	14329	*CXO* ACIS-S	13.0	0.44104
2011 Aug 24	96434-01-04-00	*RXTE* PCA	6.60	9×10^{-7}
2011 Aug 24[a]	00458907011	*Swift*/XRT (WT)	0.94	1.8×10^{-3}
2011 Aug 27	00458907012	*Swift*/XRT (WT)	1.95	1.8×10^{-3}
2011 Aug 29	96434-01-05-00	*RXTE* PCA	6.05	9×10^{-7}
2011 Aug 30	00458907013	*Swift*/XRT (WT)	2.16	1.8×10^{-3}
2011 Sep 2	96434-01-06-00	*RXTE* PCA	5.12	9×10^{-7}
2011 Sep 2[a]	00458907014	*Swift*/XRT (PC)	2.06	2.5
2011 Sep 5[a]	00458907015	*Swift*/XRT (PC)	1.72	2.5
2011 Sep 8	96434-01-06-01	*RXTE* PCA	5.52	9×10^{-7}
2011 Sep 10[a]	00458907016	*Swift*/XRT (PC)	2.01	2.5
2011 Sep 15	00032097001	*Swift*/XRT (WT)	9.09	1.8×10^{-3}
2011 Sep 18	00032097002	*Swift*/XRT (WT)	10.45	1.8×10^{-3}
2011 Sep 21	00032097003	*Swift*/XRT (WT)	7.44	1.8×10^{-3}
2011 Sep 24	00032097004	*Swift*/XRT (WT)	8.10	1.8×10^{-3}

Notes. Log of all observations used in our analysis.
[a] Excluded from the spectral analysis.

field, $B = 1.4 \times 10^{14}$ G, confirmed the magnetar nature of Swift J1834.9−0846.

Swift J1834.9−0846 is located in a field rich in high-energy sources, which include SNR W41 (Shaver & Goss 1970; Tian et al. 2007), the TeV source HESS J1834−087 (Aharonian et al. 2005), the GeV source 2FGL J1834.3−0848 (Abdo et al. 2011), and the PSR/pulsar wind nebula (PWN) candidate XMMU J183435.3−84443/CXOU J183434.9−084443 (Mukherjee et al. 2009; Misanovic et al. 2011). Attempts to understand the nature and relations between these sources had already prompted X-ray observations with *CXO* and *XMM-Newton* before the discovery of Swift J1834.9−0846 (Mukherjee et al. 2009; Misanovic et al. 2011). We have triggered additional observations of the region with both *CXO* and *XMM-Newton*. Here we describe the analyses of the *RXTE*, *Swift*, *Fermi*, and *CXO* data and compare them to the earlier observations. The *XMM-Newton* results will be reported in a separate paper. Section 2 describes the data sets presented here, and Section 3 presents the *CXO* location and discusses possible optical counterparts. We present the light curve of the persistent emission in Section 4 and the results of our timing and spectral analyses in Sections 5 and 6, respectively. Finally, we compare the properties of Swift J1834.9−0846 with those of other magnetars and discuss the possible relation of Swift J1834.9−0846 to other sources in the field in Section 7.

2. X-RAY OBSERVATIONS AND DATA REDUCTION

The field of Swift J1834.9−0846 was observed in X-rays on 29 occasions with several telescopes; the majority was in 2011, with two earlier observations in 2005 and 2009 (see Table 1). We have analyzed here 20 *Swift*/XRT observations, 8 *RXTE*/PCA observations, and 1 *CXO*/Advanced CCD Imaging Spectrometer (ACIS) observation.

2.1. Swift/XRT Data

Of the 20 *Swift*/XRT observations listed in Table 1, 4 were carried out in the Photon Counting (PC) mode and 16 in the Window Timing (WT) mode which provides much better temporal resolution (1.8 ms) at the expense of imaging. We used the HEASOFT[8] analysis tools to reduce and analyze the data. We extracted spectra from the Level 2 event data using the standard grade selection of 0–12 and 0–2 for the PC and WT mode data, respectively. For the PC mode data, we used an $r = 15''$ circle as the source region and an annulus with the same center and inner and outer radii of $30''$ and $45''$ as the background region. For the WT mode data, we extracted the source spectra using a box centered on the *CXO* location with a length of $30''$ aligned to the one-dimensional image. The background spectra were extracted with a similar size box centered far away from

[8] Version 6.10, http://heasarc.gsfc.nasa.gov/docs/software/lheasoft/

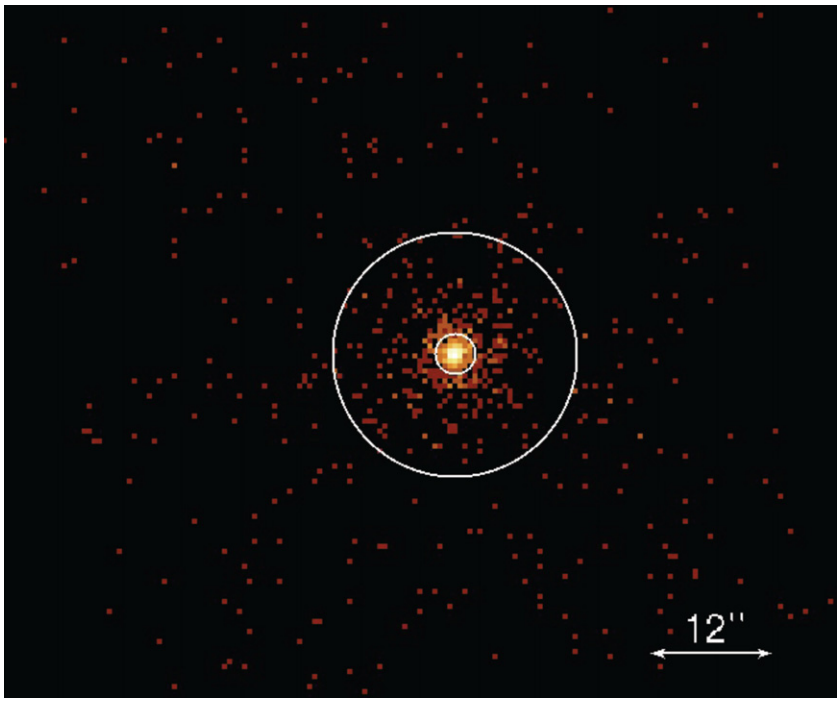

Figure 1. Image of CXOU 183452.1−084556 and surrounding emission (0.7–10 keV) obtained with ACIS-S3 on 2011 August 22. The radii of the inner and outer circles are 2″ and 12″, respectively.

(A color version of this figure is available in the online journal.)

the source. We then generated the ancillary response files with *xrtmkarf* for each spectrum and regrouped the source spectra with a minimum of 15 counts bin^{-1}. The spectral fitting was done in XSPEC 12.6.0. Since the source was relatively bright at the onset of the outburst episode, the first XRT observation in PC mode (performed during two separate spacecraft orbits) was split into two parts to uncover early spectral variations. Three observations in WT mode and three observations in PC mode were too short to allow determination of spectral parameters. These observations were, therefore, excluded from our spectral analysis.

2.2. *RXTE*/PCA Data

Swift J1834.9−0846 was observed with *RXTE* in eight pointings with a total exposure time of about 50 ks spanning over 30 days (see Table 1). The *RXTE* data were collected with the PCA (Jahoda et al. 1996) operating with two out of the five available proportional counter units in most of the observations. All data were collected in the GoodXenon mode, where each photon is time tagged with a minimum time resolution of about 1 μs. We used the PCA data primarily for timing analysis as it is not an imaging instrument, and the source intensity is relatively dim compared to the bright background X-ray emission (e.g., diffuse Galactic ridge emission and bright point sources in the 1° field of view of *RXTE*). However, we extracted the pulse peak spectrum using the longest *RXTE* pointing to investigate the source spectral behavior in a joint PCA and *CXO* analysis (see Section 6.3).

2.3. *CXO* Data

We observed Swift J1834.9−0846 on 2011 August 22 with the *CXO* ACIS operated in the Timed Exposure mode. The target was imaged near the aim point on the S3 chip using the 1/8 subarray (8′ × 1′ field of view). The data of an archival *CXO* observation (see Misanovic et al. 2011 for a description) were also analyzed, taking into account the different angular resolution and sensitivity. In our analysis, we worked with the pipeline-produced Level 2 event files (with standard filtering applied) and utilized CIAO 4.3 with CALDB 4.4.5. The spectral fitting was done in XSPEC 12.6.0.

3. SOURCE LOCATION AND OPTICAL COUNTERPART SEARCH

We used the *wavdetect* CIAO tool to determine the point sources in our *CXO* observation. In the vicinity of the *Swift*/XRT location we find a point source, which we designate CXOU J183452.1−084556, centered at R.A. = $18^{\rm h}34^{\rm m}52\overset{\rm s}{.}118$, decl. = −08°45′56.″02. We also notice the presence of extended emission, up to ≃15″ from the point source, with isotropic surface brightness distribution (see Section 6.2.2). The uncertainty of this position is dominated by the *CXO* absolute position uncertainty of 0.″6 (at 90% confidence level).[9] The *CXO* image of the vicinity of Swift J1834.9−0846 is shown in Figure 1.

We compared the *CXO* image to the archival Two Micron All Sky Survey (2MASS) images of the same region of sky. We do not detect any near-infrared (NIR) sources within 2″ distance from the position of CXOU J183452.1–084556. We also observed the field of Swift J1834.9−0846 with the Wide Field Infrared Camera (WIRC; Wilson et al. 2003) on the 5 m Palomar Hale telescope on 2011 August 23. WIRC has a field of view of 8.′7 × 8.′7 and a pixel scale of 0.2487 arcsec pixel^{-1}. We obtained seven dithered $K_{\rm s}$ band images, consisting of four co-added 30 s exposures taken at each dither position. The atmospheric conditions were very good, with seeing $\lesssim$1″ and clear skies. The individual frames were reduced in the standard manner using IRAF, calibrated and mosaicked together. The

[9] See http://cxc.harvard.edu/cal/ASPECT/celmon/.

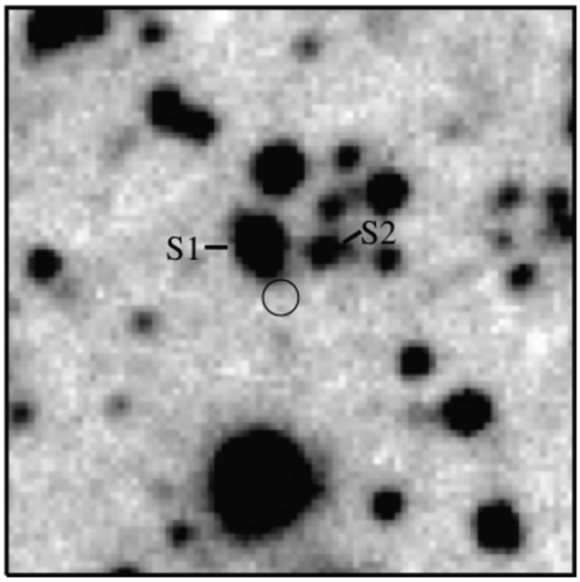

Figure 2. Palomar/WIRC K_s-band image showing the $r = 0\farcs6$ *CXO* error circle for CXOU 183452.1−084556. The sources designated as S1 and S2 are the ones reported by Levan & Tanvir (2011).

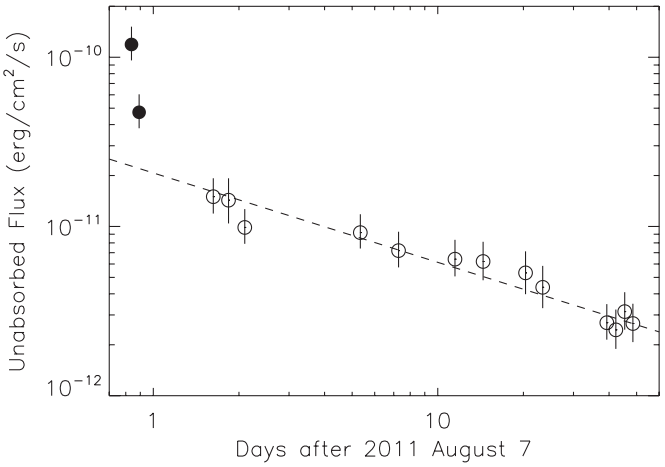

Figure 3. Persistent X-ray light curve (2–10 keV) of Swift J1834.9−0846/CXOU J183452.1−084556 obtained from 48 days monitoring of the source with *Swift*/XRT. The dashed line shows the best-fit power-law temporal decay model ($\propto t^{-0.53}$).

resulting image was astrometrically calibrated using 2MASS. The astrometric solution carries a formal 1σ error of $0\farcs1$ for the transfer of the 2MASS reference frame to the WIRC image shown in Figure 2. No sources are detected within the *CXO* error circle down to a limiting magnitude of $K_s \sim 19.5$ (at the 5σ level). The sources designated as S1 and S2 on the figure are the ones reported earlier by Levan & Tanvir (2011).

4. PERSISTENT X-RAY LIGHT CURVE OF SWIFT J1834.9−0846

Swift J1834.9−0846 was observed on 20 occasions with *Swift* after the outburst onset (see Table 1). This coverage allows us to construct a light curve of the source, which spans 48 days. In Figure 3, we present the persistent X-ray flux history in the 2–10 keV range as calculated using the power-law (PL) spectral model described in Section 6.1. The X-ray light curve of the source indicates a rapid decay in the very early episode ($\lesssim$1 day), and it is consistent with a steady flux decay over the longer term. A PL fit to the temporal decay trend (i.e., $F \propto t^{-\alpha}$) yields a good fit with $\alpha = 0.53 \pm 0.03$ and $\alpha = 0.53 \pm 0.07$ for the observed and unabsorbed fluxes, respectively. Notice that because of the limited spatial resolution, the XRT data include both the point source and the surrounding extended emission. As a consequence, the decay trend of the point source cannot be unambiguously determined from these data.

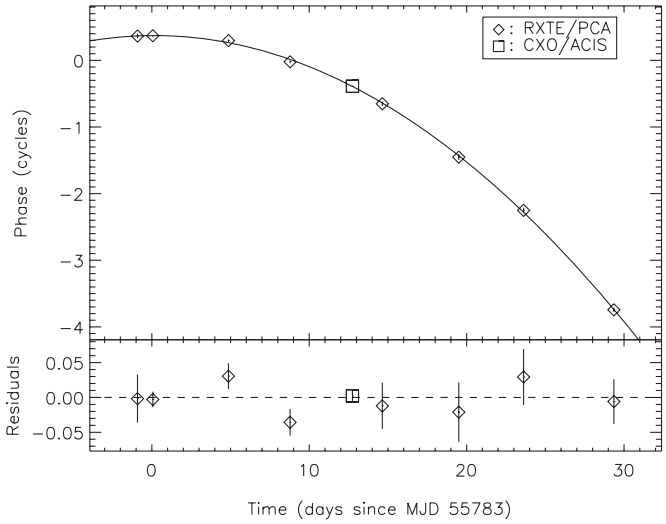

Figure 4. Top panel: plot of phase shifts for each *RXTE* observation of Swift J1834.9−0846. The solid line is a quadratic trend that fits the time evolution of the phase shifts. Bottom panel: residuals of the fit.

5. TIMING ANALYSIS

5.1. RXTE

Swift J1834.9−0846 was observed by *RXTE* on eight occasions with a total exposure time of ∼50 ks, spanning a time baseline of over 30 days (see Table 1). For our timing analysis we used data collected in the 2–10 keV range. For each observation, we first inspected the light curve with 0.03125 s time resolution and filtered out the times of short spikes and instrumental artifacts. We then converted the event arrival times to that of the Solar System Barycenter in Barycentric Dynamical Time using the JPL DE200 ephemeris and the *Swift*-derived coordinates of the source.

Next, we employed a Fourier-based pulse profile folding technique to determine the spin ephemeris of Swift J1834.9−0846. We first generated a template pulse profile by folding the longest PCA observation (Observation ID: 96434-01-02-00) at the pulse frequency determined with a Z_1^2 search (Buccheri et al. 1983). Then, we generated pulse profiles for all PCA observations as well as for the *CXO* pointing, and cross-correlated them with the template profile to determine the phase shifts with respect to the template. We obtain the spin ephemeris of the source by fitting the phase shifts with a first or a higher order polynomial. We find that the phase drifts of Swift J1834.9−0846 are best described with a second-order polynomial ($\chi^2 = 7.3$ for 7 degrees of freedom, dof) that yields a spin period $P = 2.4823018(1)$ s and a period derivative $\dot{P} = 7.96(12) \times 10^{-12}$ s s^{-1} (epoch: 55783 MJD). In Figure 4, we present the drift of the pulse phase with respect to the template and the quadratic trend curve (upper panel), and the fit residuals in cycles (lower panel). The measured values of P and $\dot{P}$ correspond to the following spin-down parameters: age $\tau = P/2\dot{P} = 4.9$ kyr, power

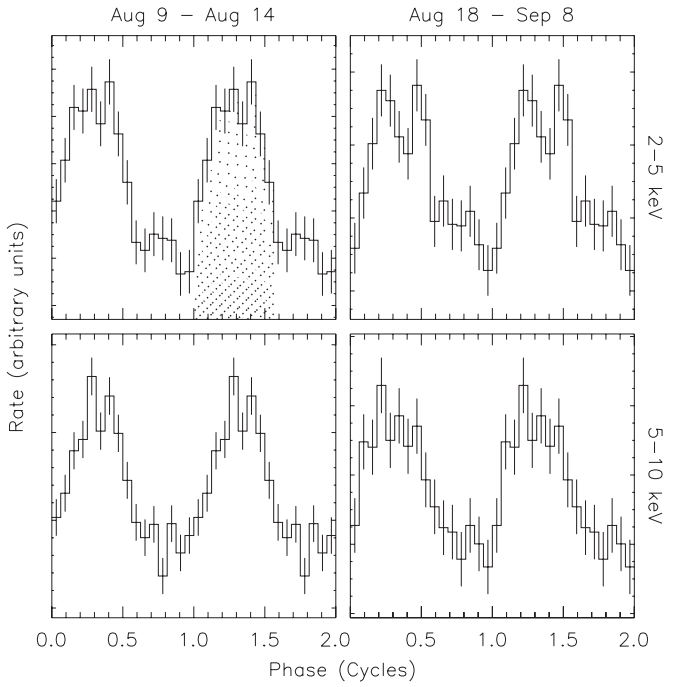

Figure 5. Dependence of the *RXTE* pulse profiles on time and energy. The shaded area in the top left panel corresponds to the phase interval used for spectral analysis (see Section 6.3).

$\dot{E} = 4\pi^2 I \dot{P} P^{-3} = 2.1 \times 10^{34}$ erg s^{-1}, and magnetic field $B = 3.2 \times 10^{19} (P\dot{P})^{1/2} = 1.4 \times 10^{14}$ G.

Finally, Figure 5 shows the pulse profiles obtained from several *RXTE* observations folded together using the derived ephemeris. We note the appearance of additional harmonics in the low-energy pulse profile of the source (2–5 keV) in *RXTE* data taken at later times.

5.2. *CXO*

We searched for pulsations in the *CXO*/ACIS data obtained in the 2011 August 22 observation. We used the 733 counts extracted from the $r = 1''$ circle around the CXOU J183452.1−084556 position in the 2–10 keV band (there are only four counts below 2 keV, likely from the background). The time resolution in this observation was 0.44104 s (0.4 s frame time plus 0.04104 s charge transfer time). The photon arrival times were transformed to the Solar System Barycenter using the CIAO *axbary* tool. The ACIS observation started at epoch 55795.6489 MJD and continued for $T_{\rm span} = 13.02$ ks.

We calculated the Z_1^2 statistic as a function of trial frequency with a step of 0.35 μHz (which is about 0.05 $T_{\rm span}^{-1}$) and found the maximum $Z_1^2 = 467$ at $\nu = 0.4028512$ Hz $\pm$ 2.0 μHz,[10] implying a very high significance of the pulsed signal. We also calculated Z_n^2 for $n > 1$ but did not find a strong contribution of higher harmonics.

Figure 6 (upper panel) shows the pulse profiles with 5 and 10 phase bins. We used these profiles to measure the pulsed fraction,[11] $p = 85\% \pm 10\%$. We estimated the uncertainty of the pulsed fraction using Monte Carlo simulations and bootstrapping, also accounting for the time resolution and dead time in the 1/8 subarray mode. We also performed randomization of the arrival times within the 0.4 s frame time and re-calculated the pulsed fraction, which remained within the uncertainty range estimated above.

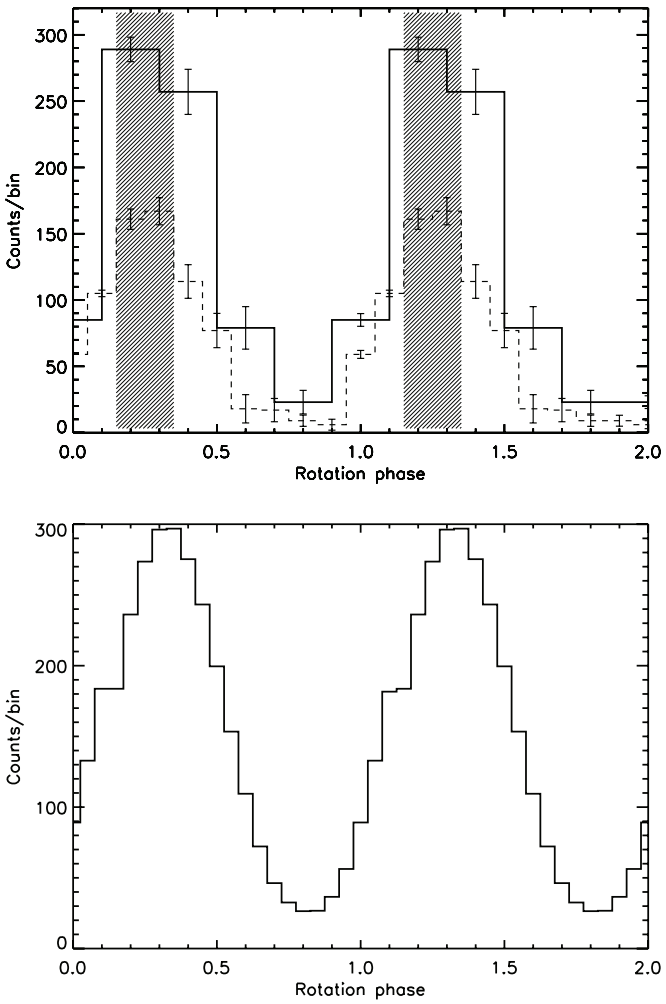

Figure 6. Top panel: *CXO* pulse profiles (2–10 keV) with 5 and 10 phase bins. The shaded regions indicate the peak interval (phases 0.15–0.35) used for phase-resolved spectroscopy. Bottom panel: *CXO* pulse profiles (2–10 keV) with 10 phase bins, averaged over the reference phase.

The pulsed fraction can also be defined as $\tilde{p} = [2(Z_n^2 - 2n)/N]^{1/2}$, where n is the number of harmonics that give a significant contribution, and N is the number of counts.[12] In our case, $\tilde{p} = 1.13$ exceeds 100%, which might be due to dead-time effects and the relatively large (≈0.18) ratio of the time resolution to the period. To measure the pulsed fraction more accurately, the target should be observed with a better time resolution.

Figure 6 (lower panel) shows a 20-bin pulse profile averaged over the reference phase.[13] We also produced a pulse profile for the surrounding extended emission but did not find a statistically significant pulsed signal.

[10] The 1σ uncertainty is calculated as $\delta\nu = 3^{1/2}\pi^{-1} T_{\rm span}^{-1} (Z^2_{1,\rm max})^{-1/2}$ (see Chang et al. 2012).

[11] The pulsed fraction p is defined as the ratio of the number of counts above the minimum level to the total number of counts.

[12] The advantage of this definition is the independence of $\tilde{p}$ of phase binning. For the case of purely sinusoidal pulsations, $\tilde{p}$ coincides with p (assuming a very large number of bins and low noise), while it is a factor of $\sqrt{2}$ larger than the rms measure of variability.

[13] This pulse profile was obtained by averaging 100 pulse profiles (20 bins each) constructed by assigning different phases to the first count and folding with the SGR period.

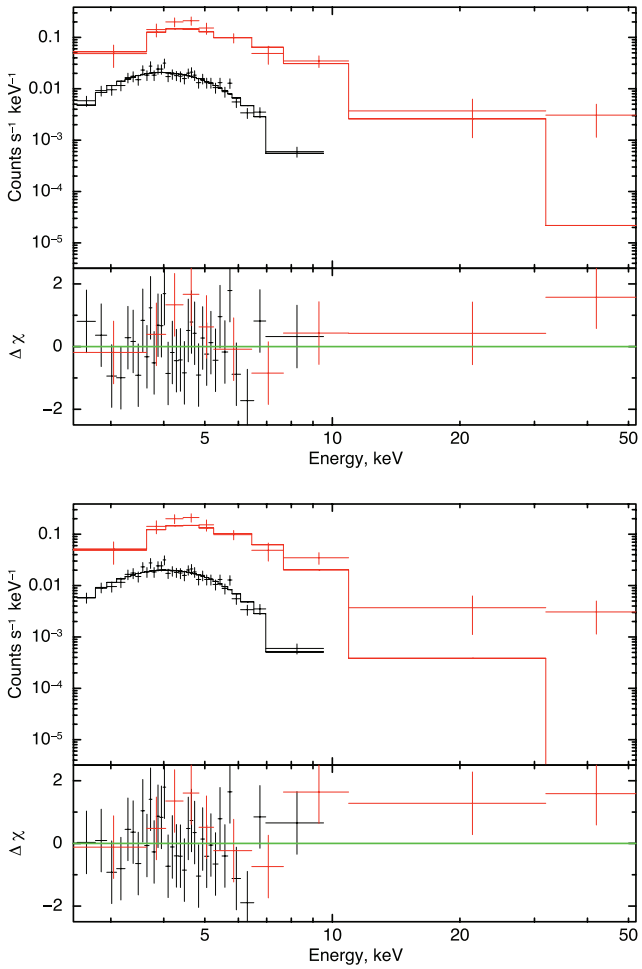

Figure 7. *CXO*/ACIS (black/bottom) and *RXTE*/PCA (red/top) spectra of CXOU 183452.1−084556 jointly fitted with the PL and BB models (top and bottom panels, respectively).

(A color version of this figure is available in the online journal.)

6. SPECTRAL ANALYSIS

6.1. Swift

We have fitted all XRT spectra (2–10 keV) jointly with two continuum models: a PL and a single blackbody (BB), both with interstellar absorption. In the first case, we find that the photon index remains the same within the uncertainties; therefore, we forced all observations in our joined fit to have the same varying photon index, while the normalizations were allowed to vary individually. We obtained a good fit ($\chi^2_\nu = 1.01$ for 62 dof) with the best model parameters $N_{\rm H} = 10.5^{+1.9}_{-1.8} \times 10^{22}$ cm^{-2}, and photon index $\Gamma = 3.2 \pm 0.4$. The absorbed BB model resulted in temperatures that also remained consistent within their uncertainties; we then linked the temperatures and allowed the normalizations to vary. We again obtained a good fit ($\chi^2_\nu = 1.04$ for 62 dof) with $N_{\rm H} = 4.4^{+1.3}_{-1.2} \times 10^{22}$ cm^{-2} and $kT = 1.1 \pm 0.1$ keV. The temperature is higher than those measured in most other magnetars (typically around 0.5 keV; Woods & Thompson 2006).

6.2. CXO

6.2.1. CXOU J183452.1−084556

We collected a total of 733 counts (2–10 keV) from a circular region of $r = 1''$ centered at CXOU J183452.1−084556; the background contribution is expected to be only 0.25 counts (background was measured an $20'' < r < 33''$ annulus). We then grouped the source spectrum requiring a minimum of 15 counts per spectral bin. The resulting spectrum is shown in Figure 7 (black error bars). The source pileup is negligibly small ($\lesssim$1%), as the total source count rate of 0.057 counts s^{-1} corresponds to 0.025 counts per frame. The point source spectrum can be fitted equally well with both the absorbed PL and BB models (see Table 2). The observed (absorbed) flux (2–10 keV) is $F_{\rm point} = (3.0 \pm 0.1) \times 10^{-12}$ erg s^{-1} cm^{-2} (corrected for the finite extraction aperture and 9% dead time). Table 2 contains the values of the $N_{\rm H}$ and photon index for the best-fit absorbed PL model, and the $N_{\rm H}$ and temperature (kT) of the BB model. From the BB fit we estimate the emitting area radius to be 0.26 km (assuming that the source is at the same distance of 4 kpc as the SNR W 41; Tian et al. 2007). The corresponding unabsorbed PL and BB fluxes (2–10 keV) are $1.6^{+0.6}_{-0.4}$ and $(5.8 \pm 0.6) \times 10^{-12}$ erg s^{-1}, respectively (see also Table 2).

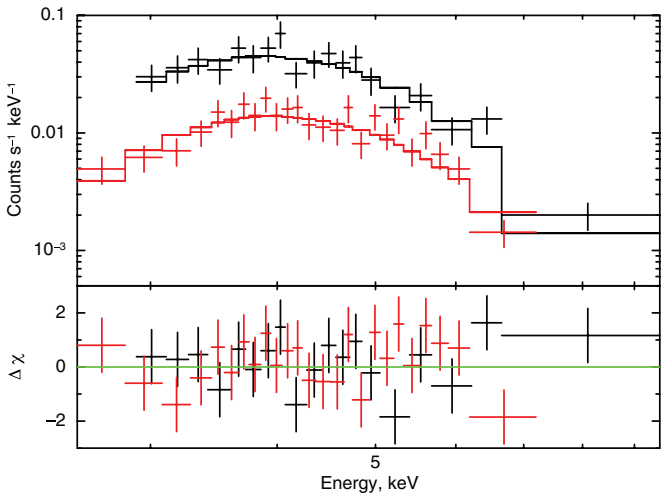

Figure 8. PL fits of the *CXO* spectra of CXOU 183452.1−084556 in the pulse maximum (black/bottom) and pulse minimum (red/top).

(A color version of this figure is available in the online journal.)

Guided by the pulse profiles shown in Figure 6, we have extracted spectra from two different phase intervals: 0.15–0.35 (peak; indicated with the shaded region in Figure 6, upper panel) and the rest (off-peak). These spectra are shown in Figure 8; we again used the PL and BB models in each case, fixing the $N_{\rm H}$ at the best-fit value of the phase-integrated spectrum. The peak and off-peak spectral parameters (Γ or kT; see Table 3) are consistent within their uncertainties.

6.2.2. Halo

We collected 314 counts (2–10 keV) from the $2'' < r < 10''$ annulus (hereafter "halo"), centered at CXOU J183452.1−084556, where the contribution of the point source is expected to be small (<10%). We subtracted the background (estimated from a much larger region away from the source) and obtained a net total of $\simeq$300 counts. To separate the halo from the point source, we simulated a point-spread function (PSF) using MARX.[14] The comparison of the data with the PSF simulation (Figure 9) shows a good agreement within a small aperture (approximately up to $1''$ radius), while the extended emission dominates at larger radii. Based on our simulation, we estimate

[14] http://space.mit.edu/cxc/marx/

Table 2
Spectral Fit Parameters of Swift J1834.9−0846 (Point Source) and its Extended Emission (Halo)

Model	$N_{H,22}$	$\mathcal{N}^a$ or R^b	Γ^c or kT^c	χ^2_ν/dof [d]	L_X[e]
CXO, PL (point)	$20.3^{+2.7}_{-2.5}$	$4.8^{+5.9}_{-2.4}$	$3.5^{+0.5}_{-0.4}$	0.72/31	3.1
CXO, BB (point)	$12.0^{+1.8}_{-1.7}$	$0.26^{+0.14}_{-0.07}$	1.1 ± 0.1	0.75/31	0.33
CXO, PL (halo)	$10.0^{+2.2}_{-2.0}$	$0.6^{+1.1}_{-0.3}$	3.7 ± 0.6	0.86/17	0.31
CXO, PL (point)	15 (fixed)	$0.83^{+0.19}_{-0.16}$	2.7 ± 0.2	0.86/32	1.7
CXO, PL (halo)	15 (fixed)	$4.8^{+2.2}_{-1.5}$	5.0 ± 0.3	1.05/18	0.67
CXO, PL (pre-outburst, halo)	$4.0^{+3.1}_{-1.9}$	$5.5^{+4.0}_{-2.5} \times 10^{-4}$	$1.0^{+0.8}_{-0.5}$	0.72/7	∼0.01
CXO, PL (pre-outburst, halo)	15 (fixed)	$4.7^{+3.2}_{-1.0} \times 10^{-2}$	3.5 ± 0.1	0.80/8	∼0.03
CXO (point) and RXTE, PL	$20.7^{+2.2}_{-2.0}$	$4.8^{+5.2}_{-2.0}$	$3.6^{+0.4}_{-0.3}$	0.77/41	2.8
CXO (point) and RXTE, BB	$10.0^{+1.7}_{-1.5}$	$0.18^{+0.10}_{-0.06}$	$1.15^{+0.09}_{-0.08}$	0.88/41	0.18

Notes. The uncertainties are given at 68% confidence level for a single interesting parameter.
[a] Spectral flux in units of 10^{-2} photons cm^{-2} s^{-1} keV^{-1} at 1 keV.
[b] BB radius in units of km^2.
[c] Photon index or BB temperature in keV.
[d] Reduced χ^2 and the number of degrees of freedom.
[e] Unabsorbed PL luminosity in the 2–10 keV band or bolometric BB luminosity ($\pi R^2 \sigma T^4$) in units of 10^{34} ergs s^{-1}.

Table 3
Power-law Fits to the Phase-resolved ACIS Spectra of Swift J1834.9−0846

Phases	$N_{H,22}$	$\mathcal{N}$ [a]	Γ [b]	χ^2_ν/dof [c]
Peak	20.3	1.5 ± 0.2	3.8 ± 0.3	0.94/40
Off-peak	20.3	0.30 ± 0.04	3.5 ± 0.2	0.94/40

Notes. N_H was held fixed during the fit. The uncertainties are given at 68% confidence level for a single interesting parameter.
[a] Spectral flux in units of 10^{-2} photons cm^{-2} s^{-1} keV^{-1} at 1 keV.
[b] Photon index.
[c] Reduced χ^2 and the number of degrees of freedom.

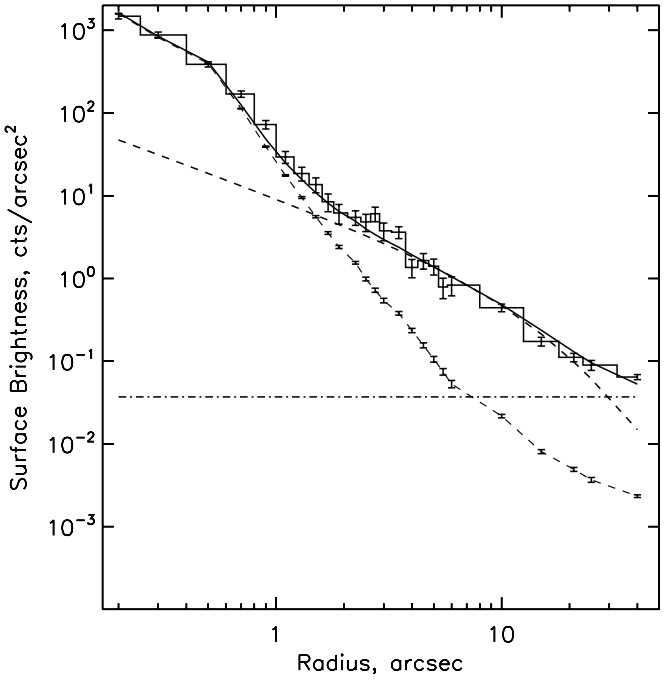

Figure 9. Radial profile in 2–10 keV from the 13 ks *CXO*/ACIS observation (histogram) shown together with the simulated PSF (dashed line with error bars), a dust halo model (dashed line) from Misanovic et al. (2011), and a background (horizontal dash-dotted line) measured from the current observation. The solid line shows the sum of all three components.

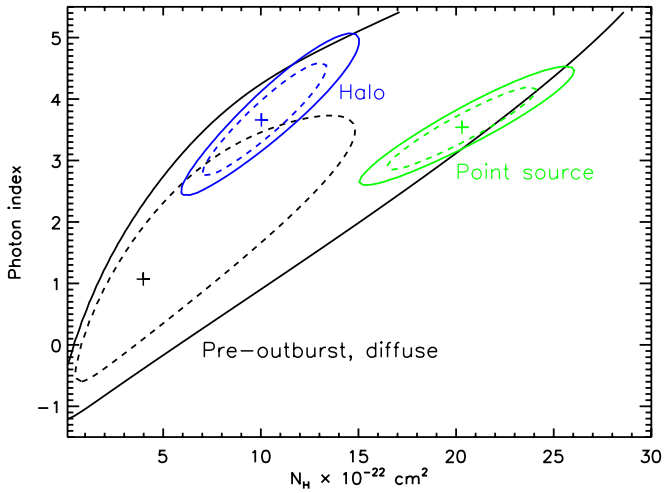

Figure 10. Confidence contours (68% and 90%) in the N_H–Γ plane for the PL fit to the halo (blue), point source (green), and the pre-outburst diffuse emission (black) spectra. The contours are obtained with the PL normalization fitted at each point of the grid. The best-fit parameter values are shown by crosses.
(A color version of this figure is available in the online journal.)

that ∼33 photons come from the point source, after taking into account the extended PSF wings. The final halo spectrum was also binned, requiring a minimum of 15 counts bin^{-1}. The best-fit PL slope is approximately the same as that of the point source spectrum, while the best-fit N_H is a factor of two lower (see Table 2). The N_H–Γ confidence contours for the halo spectrum, together with those for the point source spectrum, are shown in Figure 10. The absorbed and unabsorbed fluxes (2–10 keV) of the halo emission are $F_{halo} = (4.7 \pm 0.2) \times 10^{-13}$ and $(1.6 \pm 0.4) \times 10^{-12}$ erg s^{-1} cm^{-2}, respectively.

The extended emission is well described by the same dust halo model as the one used by Misanovic et al. (2011) for another nearby source, CXOU J183434.9−084443, according to which most of the dust must be located relatively close to the source (within 1/4 of the distance). At least part of this dust could be associated with the molecular cloud that appears to be interacting with W41 (Leahy & Tian 2008), in agreement with the very large absorption column that we find in our spectral analysis (see Table 2).

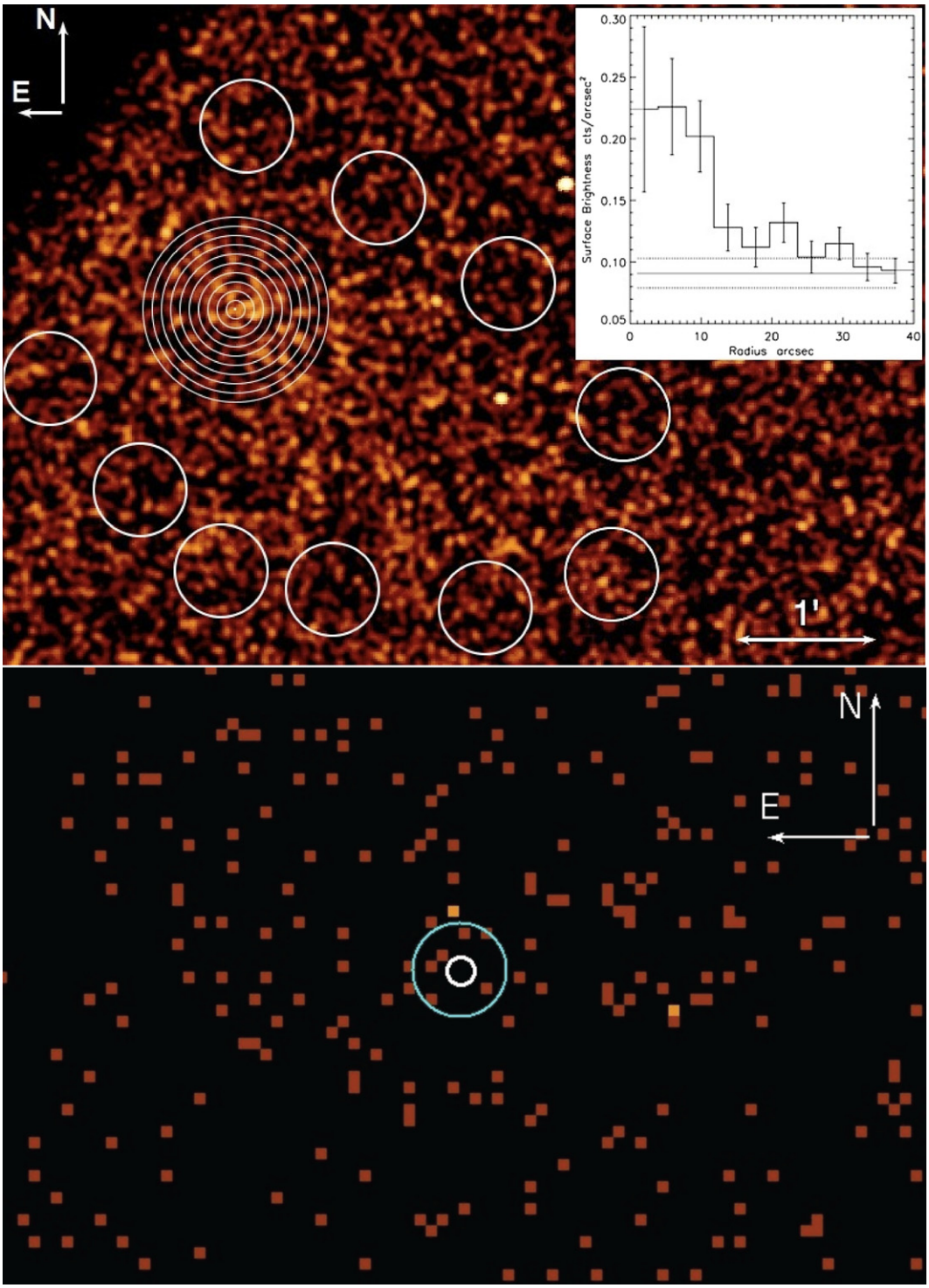

Figure 11. Archival 2–8 keV ACIS-S3 images of the CXOU J183452.1−084556 field obtained on 2009 June 7. Upper panel: binned (pixel size 0.″98) and smoothed (with a 2.″9 Gaussian kernel) image of the field. The annuli, centered at the SGR position, are used to extract the radial profile of the surface brightness distribution (shown in the inset). The background (solid horizontal line in the inset) and its uncertainty (dotted horizontal lines) are measured from the ten $r = 20''$ circular regions. Lower panel: zoomed-in image of the field around the position of CXOU J183452.1−084556 at the native ACIS-S3 binning with no smoothing applied. The circles with radii 0.″6 and 2″ were used to estimate the detection upper limit (see Section 6.2.3).

(A color version of this figure is available in the online journal.)

6.2.3. Pre-outburst CXO/ACIS Data Taken on 2009 June

We analyzed the 2009 *CXO* observation covering the Swift J1834.9−0846 field and found zero photons within the error circle ($r = 0.''6$) of CXOU 183452.1−084556 (see Figure 11). The off-axis angle of ≈4.′6 during that observation is, however, large enough for the angular resolution to be substantially degraded compared to on-axis. Hence, to estimate the 2009 upper limit on the source flux, we used a larger radius, $r = 2''$, which would contain about 50% of the flux of a point source at this off-axis angle. We found five and four photons in the 0.5–10 and 2–10 keV bands, respectively. The mean local

background surface brightness is 0.24 ± 0.02 and 0.18 ± 0.01 counts arcsec^{-2} in 0.5–10 and 2–10 keV, respectively. Thus, within the $r = 2''$ extraction aperture we would expect to detect about two counts from the background. This translates into an upper limit of 0.15 counts ks^{-1} in 2–10 keV, which corresponds to an absorbed flux limit of $F_{\rm point} < (2\text{–}4) \times 10^{-15}$ erg s^{-1} cm^{-2}.

Although we do not detect a point source, we notice extended emission on larger scales around the position of Swift J1834.9−0846. We demonstrate this by plotting the radial profile of the surface brightness (see Figure 11, top panel). The 10 annuli used to extract the radial profile are centered at the position of Swift J1834.9−0846, while the background is measured from 10 circular ($r = 20''$) regions surrounding the source. One can see from the figure inset that most of the excess over the background is within $r \lesssim 12''$ and it corresponds to a detection significance of $\approx 5.1\sigma$. However, there is also marginal ($\approx 3\sigma$) evidence for extended emission at larger scales (between $r = 12''$ and $30''$; see Figure 11, top). There might be an even more extended (primarily toward southwest from the Swift J1834.9−0846), fainter asymmetric emission, but its significance can only be established with deeper *CXO*/ACIS observations.

We also found evidence for extended emission in the 2005 *XMM-Newton* data (see also Mukherjee et al. 2009). The extent, location, and significance of the extended emission in the EPIC/MOS images (which are not affected by the chip gaps and have a low enough background) are similar to those measured from the 2009 *CXO*/ACIS images (see above). The previously reported large-scale extended emission west–northwest of the SGR (i.e., in the direction toward CXOU 183434.9−084443) could be mainly due to the point sources that are smeared out in the EPIC images because of the coarse angular resolution of *XMM-Newton*. The two brightest point sources are clearly resolved in the sharper *CXO*/ACIS images (cf. corresponding panels in Figure 11). We did not attempt to extract the spectra from the 2005 *XMM-Newton*/EPIC data because the background is much higher and the angular resolution is worse than the one of the *CXO* observation. No point source is detected in the *XMM-Newton* images at the position of CXOU J183452.1−084556. We have not estimated an *XMM-Newton* upper limit on the point source flux, as it would be less restrictive than the one derived using the 2009 *CXO*/ACIS data.

6.3. Joint Fits of CXO and RXTE Data

Since the *RXTE*/PCA is not an imaging instrument, we could not spatially separate the halo and the point source or even subtract a background measured independently from an offset region. However, since the instrument has a broader spectral range than the *Swift*/XRT and *CXO*/ACIS, potentially providing valuable source information above 10 keV, we used the latter data to calibrate our PCA spectrum of the longest (9.7 ks) pointing of 2011 August 9 (see Table 1). For the *RXTE* data, we accumulated the spectrum at the pulse minimum (which contains background, halo, and any unpulsed point source contributions) as the background and subtracted it from the source spectrum integrated over the remaining phases (see shaded regions in Figure 5). The resulting pulsed emission spectrum was then rebinned to have at least 50 counts per spectral bin after the background subtraction.

We performed a joined spectral fit of the *RXTE* (2–50 keV) and the *CXO*/ACIS (2–10 keV) data (see Figure 7). We found that the best fits are obtained when the *RXTE* flux is scaled down by a factor $\eta = 0.6$. The resulting PL best-fit parameters are very close to those of the *CXO*/ACIS fits but somewhat better constrained (see Table 2). A single BB fit is disfavored by systematic residuals at energies >8 keV (see Figure 7, bottom panel). The introduced scaling of the *RXTE* flux can be interpreted as due to two reasons: (1) the source was brighter at the time of the *RXTE* observation, and (2) the true background is lower than that estimated from the pulse minimum (see above).

7. DISCUSSION

7.1. Swift J1834.9−0846

Swift J1834.9−0846 has one of the shortest periods among magnetars[15] and one of the highest pulsed fractions of the persistent X-ray emission, similar to that of 1E 1048.1−5937 on 2000 December 28 (Tiengo et al. 2002). In its timing and spectral properties, Swift J1834.9−0846 strongly resembles the recently discovered SGR J1833−0832, which has a period of 7.6 s and a magnetic field of 1.8×10^{14} G (Göğüş et al. 2010; Esposito et al. 2011). In particular, similar to SGR J1833−0832 (and unlike most other SGRs with good-quality spectra), the 0.5–10 keV spectrum of Swift J1834.9−0846 can be fitted with a single BB model, whose temperature, $kT \simeq 1.1$ keV, is the same as that of SGR J1833−0832. The Swift J1834.9−0846 BB radius, $R = 0.26$ km, is a factor of three smaller than in SGR J1833−0832, which, however, may not be a significant difference given the poorly known distances. Another similarity between Swift J1834.9−0846 and SGR J1833−0832 is the lack of obvious spectral shape evolution with rotational phase. The phase-resolved spectra (see Figure 8) differ only in normalization, and the differences in other model parameters are not statistically significant. Despite these similarities, the post-burst flux decay trend is markedly different for the two SGRs. The unabsorbed flux of Swift J1834.9−0846 decreased as $\propto t^{-0.53\pm0.07}$ from day 2 after the burst (Figure 3), while the flux of SGR J1833−0832 remained constant for nearly 20 days before the onset of decline. We note, however, that this early constancy of the flux in SGR J1833−0832 is unusual; the enhanced persistent X-ray flux of magnetars following an outburst usually declines as a PL with an index similar to that of Swift J1834.9−0846.

Similar BB temperatures and radii were also found for SGR 0418+5729 ($P = 9.1$ s, $B < 7.5 \times 10^{12}$ G; Esposito et al. 2010) from the *Swift* XRT data taken within ∼10 days after the outburst. Also, SGR 0418+5729 exhibited a $\propto t^{-0.3}$ decay during the first 19 days and a much steeper, $\propto t^{-1.2}$, decay thereafter.

It is tempting to interpret the small emitting area of Swift J1834.9−0846 (similar to those of SGR J1833−0832 and SGR 0418+5729) as a hot spot on the NS surface. We should note that it would be very difficult to obtain such a high pulsed fraction even for a very small hot spot emitting (nearly isotropic) BB radiation because the pulsations would be washed out by the light bending in the NS gravitational field (see, e.g., Zavlin et al. 1995). If, however, we take into account that the angular distribution of radiation from a NS atmosphere has a narrow peak along the magnetic field direction (Pavlov et al. 1994), such a high pulsed fraction can indeed be explained assuming that the observed radiation emerges from a small hot spot near the magnetic pole of the NS. The fact that the light curve with such a high pulsed fraction shows only one peak per period suggests

[15] See the McGill AXP/SGR catalog: http://www.physics.mcgill.ca/~pulsar/magnetar/main.html.

that the magnetic field configuration is substantially different from a centered dipole (e.g., it could be a strongly decentered dipole, in which case the magnetic fields and the temperatures are substantially different at the two poles). We caution here that the BB model provides only an empirical description of the spectral shape. It can be used for comparison of different sources, but it may be significantly different from the actual spectrum emitted from a NS atmosphere (Pavlov et al. 1995) and possibly modified by the resonance Compton scattering in the NS magnetosphere (Nobili et al. 2008). Comparing the BB fit parameters of the three SGRs (J1834.9−0846, J1833−0832, and J0418+5729), we can conclude that they depend neither on the SGR period (in the range of 2–10 s) nor on the strength of the spin-down magnetic field (in the range of $(0.1–2)\times10^{14}$ G).

The nondetection of Swift J1834.9−0846 in the pre-outburst *CXO* data shows that the SGR flux can vary by at least a factor of $\sim10^3$ between the presumably truly quiescent level in the low state and an elevated level that has persisted, with a slow decay, for at least 6 weeks after the outburst. This suggests that there is a large number of SGRs in a quiescent state undetectable at the current level of sensitivity of X-ray observatories.

7.2. Extended Emission

At first glance, the extended emission around Swift J1834.9−0846, detected by *CXO* in 2011, looks rather unusual. Its radial distribution is consistent with that of a dust scattering halo (see Figure 9), but its spectrum shows some peculiarities. In particular, the best-fit hydrogen column density of the halo is a factor of two lower than that of the central source, while their spectral slopes are similar within statistics, instead of being steeper by $\Delta\Gamma = 1$–2, as expected for the model halo spectrum (see, e.g., Misanovic et al. 2011). A likely explanation can be derived from the breadth of the $N_{\rm H}$–Γ confidence contours and the strong correlation of these parameters. Indeed, Figure 10 shows that an intermediate $N_{\rm H} \approx 1.5\times10^{23}$ cm^{-2} corresponds to the 90% point source and halo confidence contours, and the best-fit photon indices at such $N_{\rm H}$ are $\Gamma \approx 3$ and ≈5 for the point source and halo, respectively. Thus, we believe that the dust scattering halo is the most plausible interpretation of the extended emission around Swift J1834.9−0846.

We should also note that a fainter extended emission was seen around the magnetar position in the archival *CXO* data from 2009 in which no point source was detected. Although the best-fit $N_{\rm H}$ and Γ for this pre-outburst emission are substantially smaller than those in the post-outburst data (see Table 2), the large uncertainties of these parameters make them consistent with the corresponding parameters measured for the halo in 2011. The existence of a halo in the archival data may indicate that Swift J1834.9−0846 experienced an outburst not long before the 2009 June 7 observation.

Although it seems certain that most of the extended emission is the dust-scattered emission from the magnetar, we cannot exclude the possibility that it may contain some kind of a PWN due to synchrotron radiation from relativistic electrons/positrons accelerated in the NS magnetosphere and shocked in the ambient medium. We know that in the case of rotation-powered pulsars, a typical X-ray PWN luminosity is about $10^{-4}\dot{E}$, albeit with a large scatter (Kargaltsev & Pavlov 2008). If the same relationship is valid for magnetars, we would expect $L_{\rm pwn} \sim 10^{30}$ erg s^{-1}, which would be undetectable at the presumed distance of 4 kpc. It might happen, however, that a "magnetar wind nebula" is more efficient than one created by a rotation-powered pulsar, in which case we would expect a detectable contribution. To separate it from the dust scattering halo, one should analyze several data sets obtained at different times after the outburst. We expect that the halo component flux would be changing in proportion to the point source flux (with a time lag), while the PWN component would remain constant.

7.3. Relation to SNR W41 and HESS J1834−087

The distance to Swift J1834.9−0846 still remains an open issue. As this source is located within W41, association with this SNR is certainly plausible (other SGRs were found near SNR centers; Woods & Thompson 2006), but it has not been firmly proven. Similar extreme absorption ($N_{\rm H} = 3\times10^{23}$ cm^{-2}; Misanovic et al. 2011) has been measured for the neighboring CXOU J183434.9−084443, indicating that such an absorption is not a unique feature of Swift J1834.9−0846 and hence not intrinsic to it. However, the distance to (and the origin of) CXOU J183434.9−084443 is also unknown. It could be a pulsar associated with W41 or a background active galactic nucleus located much farther. Leahy & Tian (2008) presented evidence for molecular clouds near W41, which are likely interacting with the SNR. The large absorbing column could be attributed to those clouds. At this point we can only conclude with certainty that Swift J1834.9−0846 is at the distance of 4 kpc or farther (the line of sight in that direction intersects several spiral arms). To better constrain the distance, the method of Durant & van Kerkwijk (2006) could be used; however, it requires grating observations, which are only feasible when the source is in the bright state. We note, however, that the conclusion by Durant & van Kerkwijk (2006), that all AXPs have more or less standard luminosity of 1.3×10^{35} erg s^{-1}, cannot hold for quiescent SGRs because otherwise they would have been easily seen even at the most extreme distance of 20 kpc.

The field surrounding Swift J1834.9−0846 is rich in high-energy sources (see Figures 12 and 13). This magnetar is located at the heart of SNR W41 and nearly at the center of the extended TeV source HESS J1834−087, which itself is confined to the SNR interior (see Figure 13). In addition, there is a somewhat offset *Fermi* source, 2FGL J1834.3−0848, located nearby (see Figure 13). Since the extent of HESS J1834−087 is significantly smaller than that of the SNR, the TeV emission cannot be coming from the SNR shell as it does in some other cases (Bochow et al. 2011). The only other plausible explanation is that the TeV emission is powered by relativistic electrons injected by the compact object formed after the SNR explosion. There are currently several candidates for such an object. First, a few SGRs are known to be associated with shell-type SNRs (Hurley 2000), and the central location of Swift J1834.9−0846 certainly supports such a hypothesis. On the other hand, there is no firm evidence so far that SGRs can produce copious amounts of relativistic particles similar to young rotation-powered pulsars. While there is a convincing evidence that pulsars can power relic PWNe emitting TeV γ-rays, such evidence is currently lacking for magnetars.

Among other sources possibly related to HESS J1834−087 and W41 are CXOU J183434.9–084443 (a PWN candidate discussed in detail by Misanovic et al. 2011) and the 2XMM J183417.2−084901, which is located right at the center of the *Fermi* error circle (see Figure 12, top panels). Further longer observations of this region are required to understand the connection between the sources observed in different energy domains.

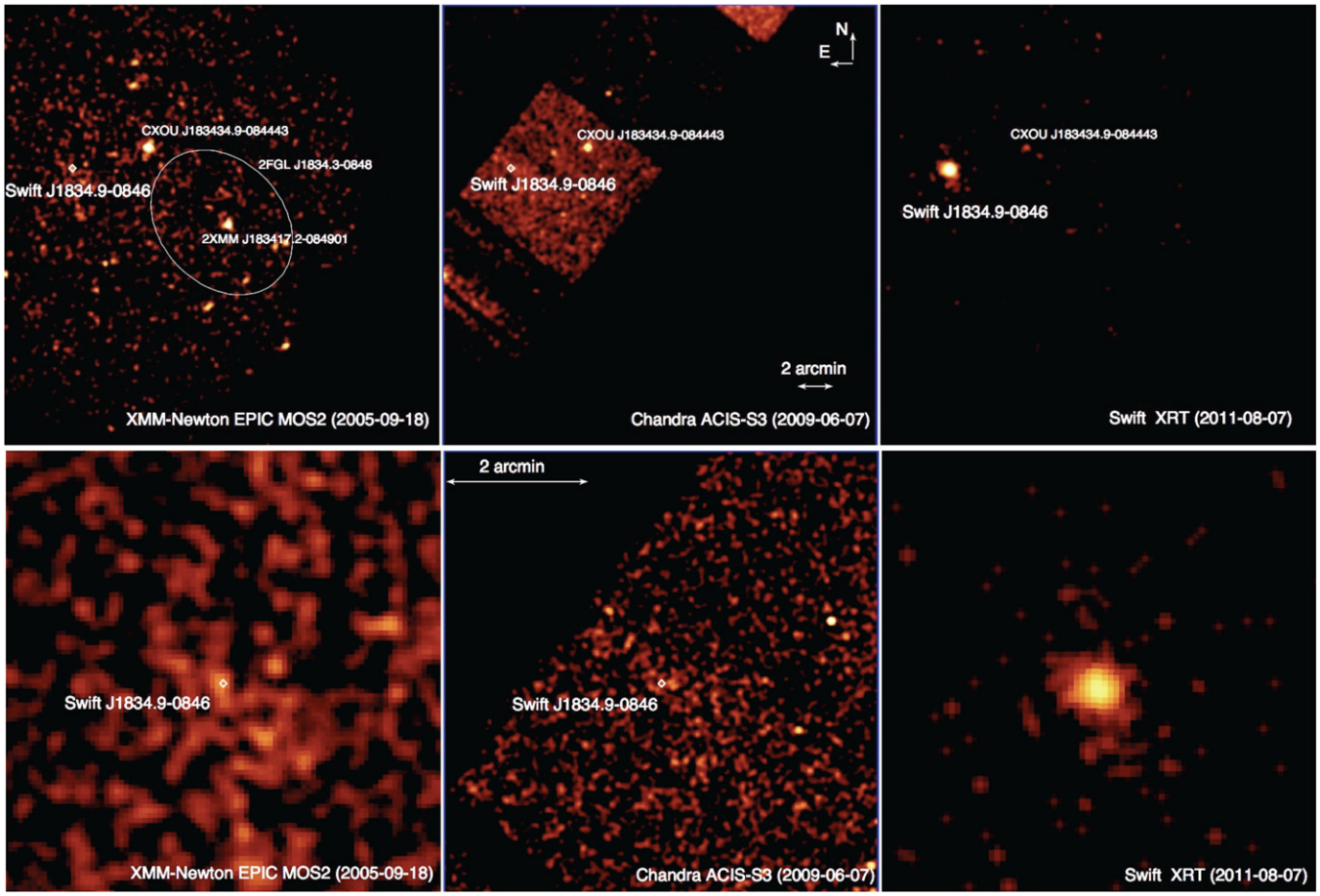

Figure 12. Mosaic of images (2–10 keV) of the central region of the W41 SNR spanning six years. The left, middle, and right columns correspond to the data obtained with *XMM-Newton*/EPIC (2005 September 18), *CXO*/ACIS-S (2009 June 7), and *Swift*/XRT (2011 August 7), respectively. The lower panels are zoomed in the Swift J1834.9−0846 position.

(A color version of this figure is available in the online journal.)

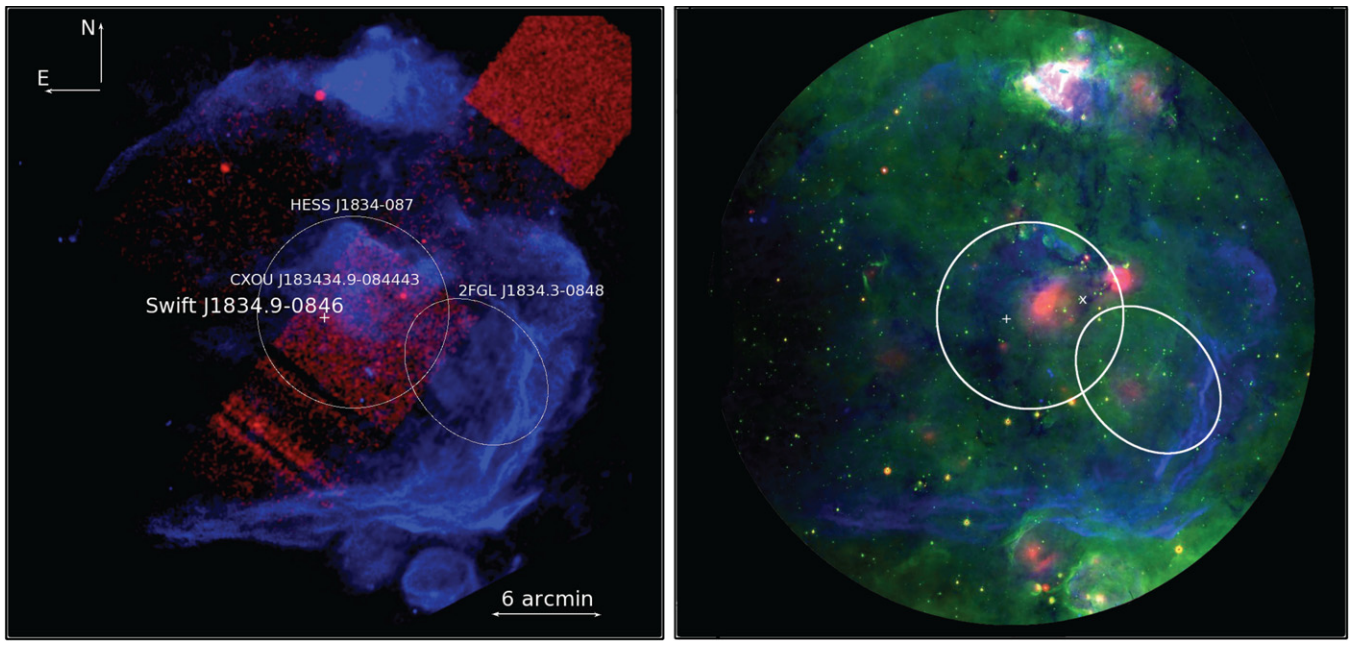

Figure 13. Multiwavelength emission from the W41 region. The left panel shows the *CXO* ACIS image (0.3–8 keV; red) and the Very Large Array (VLA) 20 cm image (blue) from the MAGPIS database (http://third.ucllnl.org/gps/). In the right panel the 20 cm VLA image is shown in blue, the *Spitzer* IRAC 8 μm image is shown in green, and the *Spitzer* MIPS 24 μm image is shown in red. The $r = 5'.4$ circle shows the extent of HESS J1834−087 (Aharonian et al. 2005); the ellipse shows the position of 2FGL J1834.3–0848 at the 95% confidence level (Abdo et al. 2011).

(A color version of this figure is available in the online journal.)

The authors are grateful to Harvey Tananbaum for his decision to award his DDT time for *CXO* observations of Swift J1834.9−0846. S.W. thanks Davy Kirkpatrick for the use of his Palomar observing time to obtain the near-IR observations of Swift J1834.9−0846. This work was partly based on observations obtained at the Hale Telescope, Palomar Observatory, as a part of a continuing collaboration between the California Institute of Technology, NASA/JPL, and Cornell University. This publication makes use of data products from the Two Micron All Sky Survey, which is a joint project of the University of Massachusetts and the Infrared Processing and Analysis Center/California Institute of Technology, funded by the National Aeronautics and Space Administration and the National Science Foundation. The work by O.Y.K. and G.G.P. was partly supported by NASA grants NNX09AC81G and NNX09AC84G, NSF grants AST09-08733 and AST09-08611, and by the Ministry of Education and Science of the Russian Federation (contract 11.G34.31.0001). C.K. was partly supported by NASA grant NNH07ZDA001-GLAST. L.L. is supported by the Postdoctoral Research Program of the Turkish Academy of Sciences (TÜBA).

REFERENCES

Abdo, A. A., Ackermann, M., Ajello, M., et al. 2011, arXiv:1108.1435
Aharonian, F., Akhperjanian, A. G., Aye, K.-M., et al. 2005, Science, 307, 1938
Barthelmy, S. D., Baumgartner, W. H., Cummings, J. R., et al. 2011, GCN Circ., 12259, 1
Bochow, A., Carrigan, S., Gast, H., & Marandon, V. 2011, Proc. 32nd ICRC (Beijing), in press (arXiv:1112.4976)
Buccheri, R., Bennett, K., Bignami, G. F., et al. 1983, A&A, 128, 245
Chang, C., Pavlov, G. G., Kargaltsev, O., & Shibanov, Y. A. 2012, ApJ, 744, 81
D'Elia, V., Barthelmy, S. D., Baumgartner, W. H., et al. 2011, GCN Circ., 12253, 1
Duncan, R. C., & Thompson, C. 1992, ApJ, 392, L9
Durant, M., & van Kerkwijk, M. H. 2006, ApJ, 650, 1070
Esposito, P., Israel, G. L., Turolla, R., et al. 2010, MNRAS, 405, 1787
Esposito, P., Israel, G. L., Turolla, R., et al. 2011, MNRAS, 416, 205
Göğüş, E., Cusumano, G., Levan, A. J., et al. 2010, ApJ, 718, 331
Göğüş, E., & Kouveliotou, C. 2011a, GCN Circ., 12267, 1
Göğüş, E., Kouveliotou, C., Kargaltsev, O., & Pavlov, G. 2011b, GCN Circ., 12302, 1
Guiriec, S., Kouveliotou, C., & van der Horst, A. J. 2011, GCN Circ., 12255, 1
Halpern, J. 2011, GCN Circ., 12260, 1
Hoversten, E. A., Barthelmy, S. D., Baumgartner, W. H., et al. 2011, GCN Circ., 12316, 1
Hurley, K. 2000, in AIP Conf. Proc. 526, Gamma-ray Bursts, 5th Huntsville Symp., ed. R. M. Kippen, R. S. Mallozzi, & G. J. Fishman (Melville, NY: AIP), 763
Jahoda, K., Swank, J. H., Giles, A. B., et al. 1996, Proc. SPIE, 2808, 59
Kargaltsev, O., & Pavlov, G. G. 2008, in AIP Conf. Proc. 983, 40 Years of Pulsars: Millisecond Pulsars, Magnetars and More, ed. C. Bassa et al. (Melville, NY: AIP), 171
Kuiper, L., & Hermsen, W. 2011, ATel, 3577, 1
Leahy, D. A., & Tian, W. W. 2008, AJ, 135, 167
Levan, A. J., & Tanvir, N. R. 2011, GCN Circ., 12266, 1
Lucas, P. W., Hoare, M. G., Longmore, A., et al. 2008, MNRAS, 391, 136
Misanovic, Z., Kargaltsev, O., & Pavlov, G. G. 2011, ApJ, 735, 33
Moskvitin, A. S., Sokolov, V. V., & Uklein, R. I. 2011, GCN Circ., 12254, 1
Mukherjee, R., Gotthelf, E. V., & Halpern, J. P. 2009, ApJ, 691, 1707
Nobili, L., Turolla, R., & Zane, S. 2008, MNRAS, 389, 989
Paczyński, B. 1992, Acta Astron., 42, 145
Pavlov, G. G., Shibanov, Y. A., Ventura, J., & Zavlin, V. E. 1994, A&A, 289, 837
Pavlov, G. G., Shibanov, Y. A., Zavlin, V. E., & Meyer, R. D. 1995, in Proc. NATO Advanced Study Institute on The Lives of the Neutron Stars, ed. M. A. Alpar, U. Kiziloglu, & J. van Paradijs (Dordrecht: Kluwer), 71
Shaver, P. A., & Goss, W. M. 1970, Aust. J. Phys. Astrophys. Suppl., 14, 133
Tello, J. C., Sota, A., & Castro-Tirado, A. J. 2011, GCN Circ., 12272, 1
Tian, W. W., Li, Z., Leahy, D. A., & Wang, Q. D. 2007, ApJ, 657, L25
Tiengo, A., Göhler, E., Staubert, R., & Mereghetti, S. 2002, A&A, 383, 182
Thompson, C., & Duncan, R. C. 1995, MNRAS, 275, 255
Thompson, C., & Duncan, R. C. 1996, ApJ, 473, 322
Wilson, J. C., Eikenberry, S. S., Henderson, C. P., et al. 2003, Proc. SPIE, 4841, 451
Woods, P. M., & Thompson, C. 2006, in Compact Stellar X-ray Sources, ed. W. Lewin & M. van der Klis (Cambridge Astrophysics Ser. 39; Cambridge: Cambridge Univ. Press), 547
Zavlin, V. E., Shibanov, Y. A., & Pavlov, G. G. 1995, Astron. Lett., 21, 149